

# Flattening Gamma: Radiometric Terrain Correction for SAR Imagery

David Small, *Member, IEEE*

**Abstract**—Enabling intercomparison of synthetic aperture radar (SAR) imagery acquired from different sensors or acquisition modes requires accurate modeling of not only the *geometry* of each scene, but also of systematic influences on the *radiometry* of individual scenes. Terrain variations affect not only the *position* of a given point on the Earth's surface but also the *brightness* of the radar return as expressed in radar geometry. Without treatment, the hill-slope modulations of the radiometry threaten to overwhelm weaker thematic land cover induced backscatter differences, and comparison of backscatter from multiple satellites, modes, or tracks loses meaning. The ASAR & PALSAR sensors provide state vectors and timing with higher absolute accuracy than was previously available, allowing them to directly support accurate tie-point-free geolocation and radiometric normalization of their imagery. Given accurate knowledge of the acquisition geometry of a SAR image together with a digital height model (DHM) of the area imaged, radiometric image simulation is applied to estimate the local illuminated area for each point in the image. Ellipsoid-based or sigma naught ( $\sigma^0$ ) based incident angle approximations that fail to reproduce the effect of topographic variation in their sensor model are contrasted with a new method that integrates terrain variations with the concept of gamma naught ( $\gamma^0$ ) backscatter, converting directly from beta naught ( $\beta^0$ ) to a newly introduced terrain-flattened  $\gamma^0$  normalization convention. The interpretability of imagery treated in this manner is improved in comparison to processing based on conventional ellipsoid or local incident angle based  $\sigma^0$  normalization.

**Index Terms**—Radar cross sections, radar scattering, radar terrain factors.

## I. INTRODUCTION

THE normalization of synthetic aperture radar (SAR) imagery for systematic terrain variations is required for meaningful multi-sensor or even single-sensor multi-track intercomparisons. Accurate backscatter estimates enable more robust use of the retrieved values in applications such as the monitoring of deforestation, land-cover classification, and delineation of wet snow covered area. Accurate estimates of backscatter in the presence of severe terrain furthermore relax constraints on same-orbit exact-repeat observations for change detection: this enables shorter temporal intervals between observations, especially given wide swath imagery, and also opens

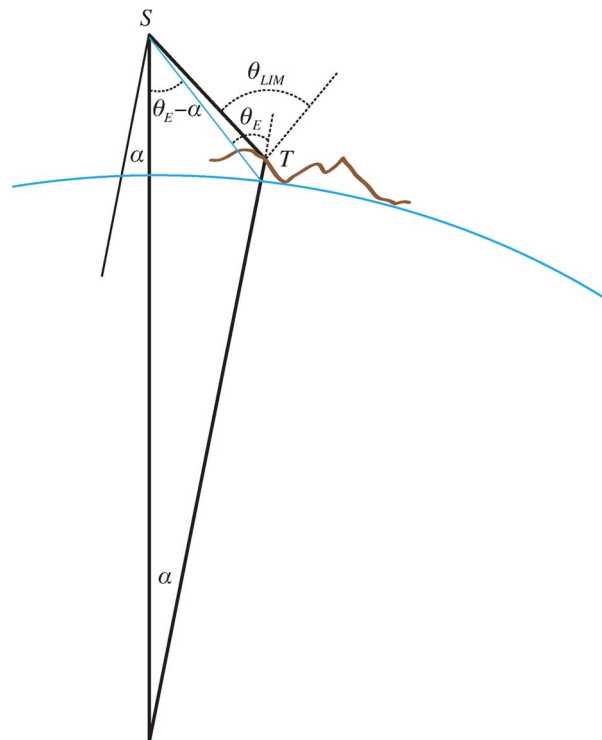


Fig. 1. Spaceborne SAR imaging geometry.

the door to multi-sensor backscatter overlays. If the local terrain is ignored due to either lack of DHM-availability or runtime-constraints leading to a need for a simpler Earth model, then the quality of the retrievable backscatter estimate is compromised. This paper extends prevailing traditional concepts of backscatter normalization, introducing a new standard known as terrain-corrected gamma naught.

To extend the concept of backscatter coefficients, it is first necessary to shortly review the existing conventions. After their introduction, the method for retrieving terrain-flattened gamma is described. Finally, results achieved using the new method are compared to conventional backscatter retrieval algorithms that either (a) use an ellipsoid Earth model, or (b) attempt slope-normalization using the local-incident angle metric.

The geometry of a spaceborne SAR is shown in Fig. 1 (not to scale). A target  $T$  on the Earth's surface is imaged from a SAR sensor at position  $S$ . The incident angle estimate differs depending if a simple *ellipsoid*( $\theta_E$ ) or alternatively a *terrain* model ( $\theta_{LIM}$ ) is used. In the case of airborne sensors, the nadir-target angle  $\alpha$  is often approximated as zero: this is not advisable in the spaceborne case. The off-nadir angle is  $\theta_E - \alpha$ .

Manuscript received April 24, 2010; revised January 9, 2011; accepted February 6, 2011. Date of publication April 21, 2011; date of current version July 22, 2011. This work was supported in part by the European Space Agency under ESRIN/Contract No. 22501/09/I-EC.

The author is with the Remote Sensing Laboratories, University of Zürich, CH-8057 Zürich, Switzerland (e-mail: david.small@geo.uzh.ch).

Color versions of one or more of the figures in this paper are available online at <http://ieeexplore.ieee.org>.

Digital Object Identifier 10.1109/TGRS.2011.2120616

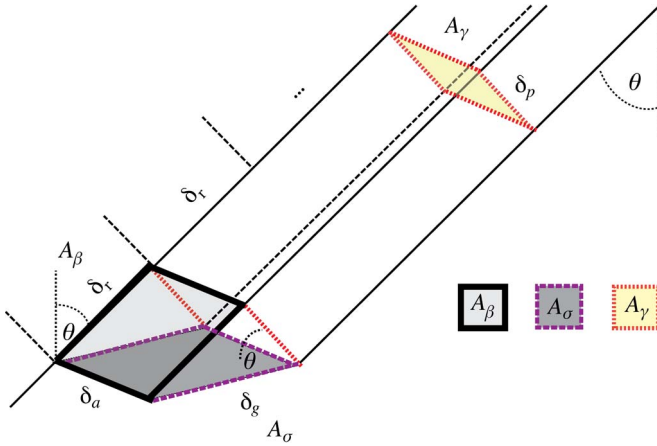


Fig. 2. Normalization areas for SAR backscatter.

### A. Backscatter Conventions

Radar backscatter  $\beta$  is expressed as a ratio between the scattered power  $P_s$  and incident power  $P_i$  at ground level:  $\beta = P_s/P_i$ . For distributed targets, the backscatter coefficient provides a backscatter ratio estimate per given reference area. Three conventional reference areas are illustrated in Fig. 2. When one chooses a reference area  $A_\beta$  (solid rectangle) defined to be in the slant range plane, one speaks of radar brightness, or *beta naught*  $\beta^0$  backscatter [11]

$$\beta^0 = \beta/A_\beta. \quad (1)$$

If the reference area is defined to be *ground area*, i.e., locally tangent to an ellipsoidal model of the ground surface  $\underline{A}_\sigma$  (dashed rectangle), then the result is *sigma naught*  $\sigma_E^0$

$$\sigma_E^0 = \beta^0 \cdot \frac{A_\beta}{\underline{A}_\sigma} = \beta^0 \cdot \sin \theta_E. \quad (2)$$

If the reference area is instead defined to be in the plane perpendicular to the line of sight from sensor to an ellipsoidal model of the ground surface  $\underline{A}_\gamma$  (dotted rectangle), then *gamma naught*  $\gamma_E^0$  is the result

$$\gamma_E^0 = \beta^0 \cdot \frac{A_\beta}{\underline{A}_\gamma} = \beta^0 \cdot \tan \theta_E. \quad (3)$$

Guidelines for transformations from a SAR product's digital number (DN) to backscatter generally follow the above equations (ASAR [12], PALSAR [2], [14]). Note that a model of the Earth is required to gain knowledge of the incident angle  $\theta_E$  to calculate sigma or gamma naught. The subscript  $E$  indicates that an ellipsoidal Earth model is used; likewise, the lower line in  $\underline{A}_\sigma$  and  $\underline{A}_\gamma$  indicates that such a “flat Earth” assumption is operative. Note that no Earth model is required to calculate  $\beta^0$  using  $A_\beta$ . The beta naught convention is usually preferable for use as the “native” radar brightness estimate in the initial processing of SAR imagery [11], as it gives the best unencumbered estimate of what the radar actually measured.

The  $\sigma_E^0$  or  $\gamma_E^0$  backscatter values may be terrain-geocoded using a digital height model (DHM), i.e., resampled into a map geometry, producing a geocoded-terrain-corrected (GTC) product [9]. It is important to understand that although the position, or *geometry* of the backscatter estimate has been

corrected in GTC products, the *radiometry* of the resulting image remains ellipsoid-model based.

### B. Shortcomings of Local Incident-Angle Mask-Based Normalization

Given the relation in (2) and (3) of backscatter to incident angle, it has been natural to consider normalization for the effects of local terrain variation using the *local* rather than *ellipsoidal* incident angle  $\theta$ . Indeed, this has been common practice for decades in the literature—see [1], [3], [5], [7], [10], [22] for representative examples.

In such “angular slope correction” approaches, one uses the relation between the ground range resolution  $\delta_g$  and the slant range resolution  $\delta_r$

$$\delta_g = \delta_r / \sin \theta. \quad (4)$$

Following from the above, one might reason that one may therefore generate a “terrain-flattened” estimate of sigma naught by removing the ellipsoid-based area normalization based on  $\theta_E$  applied by default (2), replacing it with a more appropriate area estimation using the local incident angle mask  $\theta_{LIM}$

$$\sigma_T^0 = \beta^0 \cdot \frac{A_\beta}{A_\sigma} = \sigma_E^0 \cdot \frac{\sin \theta_{LIM}}{\sin \theta_E} \quad (5)$$

where the ratio of sine terms [7] provides a slope correction factor (SCF). This normalization is referred to as “NORLIM” later in the paper.

In this paper, it is argued that such angle-based normalizations are flawed in that their sensor model fails to account for many important properties of radar backscatter in regions with significant topographic variation. Angular methods are deficient in failing to adequately model the many-to-one and one-to-many nature of the relationship between the topologies of radar slant range and DHM map geometries, so foreshortened and layover regions are modeled inaccurately [15]. Foreshortening, layover, shadow, and variations in the local reference area (also known as local sensor resolution) on fore- and back-slopes are either ignored or incorrectly modeled. Given such a poor sensor model, inaccurate backscatter estimates must and do result.

The sensor model applied in terrain normalization should account for foreshortening and layover, as their existence is a hallmark of SAR imaging. A standardized definition of reference area should be applied. In the following sections, a new terrain-flattened gamma product that avoids the long favored lossy transfer into the angular  $\theta$  domain (where terrain facet length can become singular) is advanced. This terrain flattening methodology stays in the 3-D space actually imaged by SARs, *spatially* integrating through a reference DHM to determine the local illuminated area at each radar geometry position and applying that local reference area in the normalization process.

One can argue that the classical equations (2) and (3) used to retrieve radar backscatter are adequate when dealing with images of the flatlands of Kansas, but both they and (5) use inappropriate reference areas in hilly or mountainous terrain. It is time that the standard radar backscatter retrieval equations used by the radar community left behind simplifying assumptions born in the flatlands.

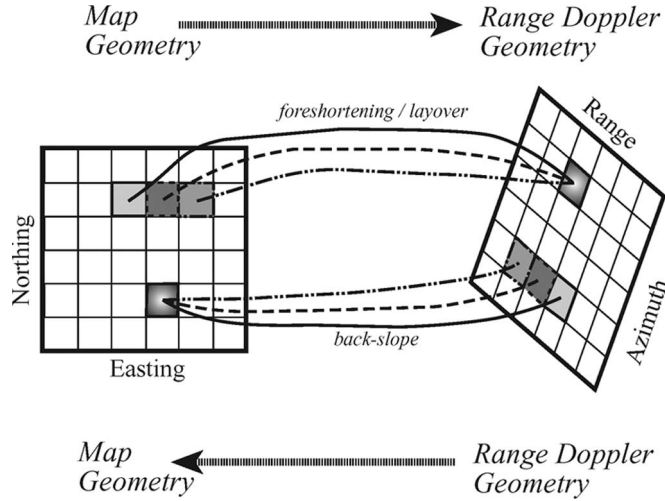


Fig. 3. Topology of radar geometry in rough topography.

## II. TIME TO LEAVE KANSAS

### A. Radar Equation

At the genesis of the conceptualization of backscatter, sigma naught was originally defined to be the ratio of backscattered power  $P_s$  to incident power  $P_i$  integrated over the area illuminated. The received power  $P_r$  is related to the transmitted power  $P_t$  as follows [21]:

$$\bar{P}_r = \frac{\lambda^2}{(4\pi)^3} \cdot \int_{\text{area illuminated}} \frac{P_t G^2}{R^4} \cdot \sigma^0 dA \quad (6)$$

where  $\lambda$  is the radar wavelength,  $G$  the one-way antenna gain,  $R$  the slant range, modeling the transformations from  $P_s \rightarrow P_r$  and  $P_t \rightarrow P_i$ . The variable of integration  $dA$  is *ground area*. The *act of integration* has usually been ignored in the literature, with the analytical solution on a planar surface implicitly substituting for a scene-specific evaluation that would include terrain influences.

### B. Lack of Homomorphism

The topological relationship between map and slant range radar geometry is illustrated in Fig. 3 for both fore- and back-slopes [15]. Given radar and map geometry grids defined to have nominally equal ground resolutions in flat terrain, bijectivity is not preserved in regions with sloped terrain. On mountain slopes facing the sensor position (fore-slopes) multiple *map geometry* grid locations are foreshortened (or even laid over) to share a single *radar geometry* grid space. The opposite occurs on mountain back-slopes on the far side of hills: multiple *radar geometry* grid locations are co-located within a single *map geometry* grid space. Mathematically, when one-to-one relationships exist between two spaces, they are bijective, or *homomorphic*. When instead *many-to-one* and *one-to-many* relationships exist between two spaces, they are not bijective, and may be described as non-homomorphic, or alternatively *heteromorphic*.

```

• Read available state vector information ( $S_x, S_y, S_z$ ) & ( $V_x, V_y, V_z$ )

• Initialize azimuth sensor position and velocity look-up tables (LUTs):
  Interpolate ( $S_x, S_y, S_z$ ) & ( $V_x, V_y, V_z$ ) to generate
   $SensorPos[1..Height_{az}]$  and  $SensorVel[1..Height_{az}]$ 

Initialize circular buffer to hold DHM row  $N$ 
for ( $N = N_0$  to  $N_1$  step  $\Delta N$ )
  • Update DHM raster index  $I_N$ 
  • Update circular buffer for DHM row  $N$ , positions from  $E_0$  to  $E_1$ 
  for ( $E = E_0$  to  $E_1$  step  $\Delta E$ )
    • Update DHM raster index  $I_E$ 
    • Retrieve local height  $h$  from DEM at index position ( $I_E, I_N$ )
    • Convert map coordinate ( $T_E, T_N, T_h$ ) to global Cartesian ( $T_x, T_y, T_z$ )
    • Point geo-location (see II.C)
      • Determine spacecraft position within  $SensorPos$  LUT fulfilling
        Doppler condition with point ( $T_x, T_y, T_z$ )  $\rightarrow t_T \rightarrow I_a$ 
      • Calculate slant range:  $R = |SensorPos(I_a) - (T_x, T_y, T_z)|$ 
      • Calculate slant range raster index:  $I_r = \lfloor R - R_0 \rfloor / \delta_r$ 
    • Calculate illuminated area estimate  $A_\gamma(I_r, I_a)_{E,N}$  (see II.E)
    • Check if locally in shadow
    If not in shadow, then
      Add area estimate  $A_\gamma(I_r, I_a)_{E,N}$  to buffer in (see II.F)
      neighborhood of  $A_\gamma(I_r, I_a)$  using bilinear distribution
    end for
  end for
  • Normalize  $A_\gamma$  for standard ellipsoid area, converting to area factor  $\hat{A}_\gamma$ 
  • Write out radar geometry simulated image  $\hat{A}_\gamma$  binary raster
  • Write out parameter annotations for simulated image  $\hat{A}_\gamma$ 

```

Fig. 4. Area integration algorithm.

### C. Terrain Geolocation

To adequately model the non-homomorphic nature of the relationship between map and radar geometry, one must integrate through a DHM. Fig. 4 lists pseudocode detailing the steps required to discretely add the individual area parcels calculated at each DHM grid location. A DHM with a resolution equal or better than that of the SAR imagery being treated is assumed in this paper. Investigation of deteriorations in simulation quality when a DHM of poorer resolution is used (see [15]) is beyond the present scope.

First, a look-up table (LUT) is constructed for each azimuth time in the radar image. An image buffer  $A_\gamma$  is allocated and initialized to zero. One chooses the appropriate order to traverse the DHM [9] to ensure that shadow is detected in a single pass. Next, the digital height model (DHM) is opened, and one begins traversal of the DHM in the chosen order. A circular buffer holding two adjacent rows is filled. The map geometry position of each point in the buffer is transformed from the DHM's cartographic or geographic reference into the global Cartesian reference frame of the sensor's state vectors. The Cartesian position is used to solve the Doppler equation [8], [9] for the appropriate reference value annotated in the radar data, providing the azimuth time  $t_T$  when the position was imaged. The distance between the sensor position at that time and the DHM position provides the slant range value  $R$ . For slant range images,  $t_T$  and  $R$  may be translated into sample index values as follows:

$$I_a = (t_T - t_0) / \delta_t \quad (7)$$

where  $I_a$  is the image's azimuth sample index,  $\delta_t$  is the line time interval, and  $t_0$  is the image's azimuth start time. Likewise, the



image's slant range index is calculated as

$$I_r = |R - R_0|/\delta_r \quad (8)$$

where  $I_r$  is the image's range sample index,  $\delta_r$  is the range sample interval, and  $R_0$  is the image's near range value.

#### D. Geocoded-Terrain-Corrected (GTC) Resampling

Once the correspondence between the local DHM position and slant range geometry is known, one could output the local backscatter estimate at the current map geometry easting and northing coordinate  $(I_E, I_N)$ , as

$$\gamma_E^0(I_E, I_N) \leftarrow \gamma_E^0(I_r, I_a). \quad (9)$$

The assignment above is performed during GTC product generation: but note that no radiometric terrain-normalization is performed when the above backscatter resampling process is chosen. In the following, we detail further steps that are required to estimate the local illuminated reference area.

#### E. Area Integration for Image Simulation

At each DHM grid location, after ensuring that the current facets are not in radar shadow, one adds the local facet area to the running tally held in the buffer  $A_\gamma$

$$A(I_r, I_a) \leftarrow A(I_r, I_a) + A(I_r, I_a)_{E,N} \quad (10)$$

where  $A$  is the area locally estimated for the current facet. The above is similar to "increasing the response level of an output grid point by a constant increment each time a DEM sub-sample is mapped to it" [4]; however, as described below, three significant refinements are added. In addition to (a) the shadow check previously mentioned [9], in the following, details are provided on (b) how to calculate the local area in the plane appropriate for providing a normalization reference for terrain-flattened gamma naught (i.e.,  $A = A_\gamma$ ), and (c) a more precise method to distribute the area estimated in Cartesian space into radar geometry (range  $\times$  azimuth).

To calculate a terrain gradient, one must consider a DHM posting together with neighbors, e.g., to the east and north. By additionally considering a further posting positioned diagonally to the east and north, one forms two terrain facets, marked as the triangles  $T_{00} - T_{10} - T_{01}$  and  $T_{11} - T_{10} - T_{01}$  in Fig. 5.

To replicate the normalization inherent to the definition of  $\sigma^0$ , one could calculate the ground area of the triangles  $E_{00} - E_{10} - E_{01}$  and  $E_{11} - E_{10} - E_{01}$  without considering the variations in area caused by the terrain facets. However, with the goal of flattening the effect of topography, one considers instead the facets  $T_1$  and  $T_2$  defined by the triangles  $T_{00} - T_{10} - T_{01}$  and  $T_{11} - T_{10} - T_{01}$  seen in Fig. 5.

To conform to the definition of  $\gamma^0$  backscatter, the area of the terrain facet triangles should first be projected onto the plane perpendicular to the local slant range direction. To the author's knowledge, projection of a DHM into this plane for normalization purposes has not been published previously. In Fig. 6, one sees how the facet edges of  $T_1(T_{00} - T_{01} -$

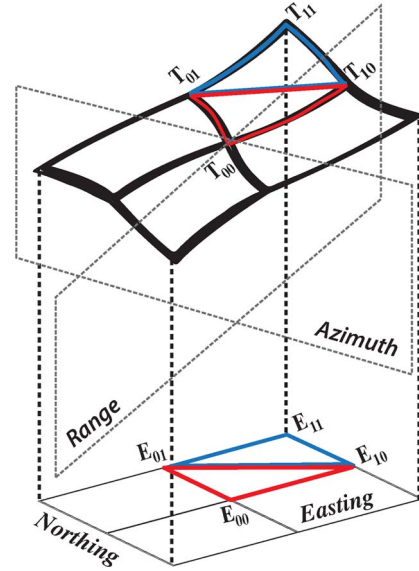


Fig. 5. DHM facet neighborhood.

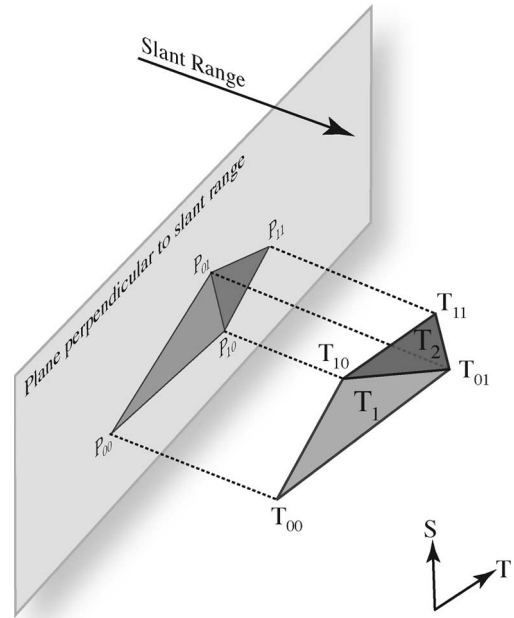


Fig. 6. Projection of DEM facets into viewing plane.

$T_{00} - T_{10} - T_{01}$ ) are projected onto the plane normal to slant range, making the triangle  $P_1$  with vertices  $(P_{00}, P_{10}, P_{01})$  and edges  $(P_{00} - P_{01} - P_{00} - P_{10} - P_{01})$ . Likewise, the second terrain facet  $T_2(T_{11} - T_{10} - T_{01})$  is projected, forming the triangle  $P_2$  with vertices  $(P_{11}, P_{10}, P_{01})$  and edges  $(P_{11} - P_{01} - P_{11} - P_{10} - P_{01})$ .

The sum of the area of the two triangles  $P_1$  and  $P_2$  is

$$A_\gamma(E, N) = A_{P_1} + A_{P_2} = A_{P_{00}-P_{01}-P_{10}} + A_{P_{11}-P_{01}-P_{10}}. \quad (11)$$

The semi-perimeters of the triangles  $P_1$  and  $P_2$  are

$$h_1 = \frac{1}{2} \cdot (P_{00-01} + P_{00-10} + P_{10-01}) \quad (12)$$

$$h_2 = \frac{1}{2} \cdot (P_{11-01} + P_{11-10} + P_{10-01}) \quad (13)$$

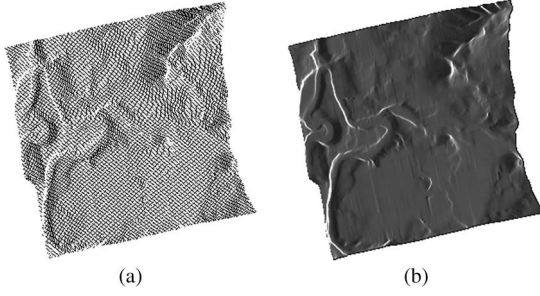


Fig. 7. Distribution of area from Cartesian into radar geometry. (a) Nearest neighbor; (b) bilinear oversampled.

For each DHM facet at a given easting  $E$  and northing  $N$  coordinate, the corresponding local illuminated area  $A_\gamma$  may then be calculated using Heron's formula

$$\begin{aligned} A_\gamma(E, N) &= A_{P_1} + A_{P_2} \\ &= \sqrt{h_1 \cdot (h_1 - P_{00-01}) \cdot (h_1 - P_{00-10}) \cdot (h_1 - P_{10-01})} \\ &\quad + \sqrt{h_2 \cdot (h_2 - P_{11-01}) \cdot (h_2 - P_{11-10}) \cdot (h_2 - P_{10-01})}. \end{aligned} \quad (14)$$

#### F. Bilinear Distribution

As explained in Section II-C, the azimuth and range indices of the input radar geometry image are derived via geolocation for a point on the Earth's surface  $T$ . Once those indices are known, the area for that grid point in the DHM may be resampled from *map geometry* into the *radar geometry* in question. Two resampling/distribution methods are available to place the area estimate into the output radar geometry desired. Results from both methods are shown in Fig. 7: nearest neighbor (*NN*) on the left, and bilinear oversampled (*BI*) on the right. The oversampling refers to decreasing the map geometry sample intervals  $\Delta E$  and  $\Delta N$  by an integer factor below that of the native DHM file.

The *NN*-approach is similar to previously published methods [4] and not explained further here. In the bilinear distribution method introduced in this paper, the four neighboring values surrounding the (fractional) coordinate  $(I_r, I_a)$  contribute to the estimate made for that location. The neighboring grid points are identified

$$I_r^0 = (\text{int})(I_r) \quad (15)$$

$$I_r^1 = I_r^0 + 1 \quad (16)$$

$$I_a^0 = (\text{int})(I_a) \quad (17)$$

$$I_a^1 = I_a^0 + 1 \quad (18)$$

with  $(\text{int})$  indicating a truncation operation whereby the largest integer smaller than the value input is returned. Linear weights scaled from zero to one encapsulate the distance to each neighboring "corner"

$$W_r = I_r - I_r^0 \quad (19)$$

$$W_a = I_a - I_a^0 \quad (20)$$

$$W_r^c = 1 - W_r \quad (21)$$

$$W_a^c = 1 - W_a \quad (22)$$

Applying the weights, the running sums of the local illuminated area in the "neighborhood" are each updated proportionately, as the area is *distributed* to the four neighbors

$$\begin{aligned} \begin{bmatrix} A_{I_r^0, I_a^0} & A_{I_r^1, I_a^0} \\ A_{I_r^0, I_a^1} & A_{I_r^1, I_a^1} \end{bmatrix} &\leftarrow \begin{bmatrix} A_{I_r^0, I_a^0} & A_{I_r^1, I_a^0} \\ A_{I_r^0, I_a^1} & A_{I_r^1, I_a^1} \end{bmatrix} \\ &+ \begin{bmatrix} W_r^c \cdot W_a^c & W_r \cdot W_a^c \\ W_r^c \cdot W_a & W_r \cdot W_a \end{bmatrix} \cdot A_{E, N} \end{aligned} \quad (23)$$

This approach is qualitatively superior to the *NN*-methodology, as although it comes at a slightly higher computational cost, it better fractionally distributes the areal estimate across multiple samples in radar geometry.

In addition to the improved fidelity achieved by using the above method to distribute the map geometry area appropriately in radar geometry, one may oversample the DHM to parcel out smaller parts of each facet piecemeal. Better yet, when available, one may directly make use of a DHM with a native resolution higher even than the (nominal) resolution of a radar image being simulated. The spatial resolution of a radar image is always provided for a nominal flat Earth (ellipsoid model) case—yet clearly, the local resolution in a radar image is typically higher than that nominal value on mountain backslopes (when not in shadow), and lower on foreslopes subject to foreshortening or even layover (see Fig. 3). Employing the most highly resolved DHM available enables appropriate use of the best available information content within the image simulation, while the oversampling option ensures that the more highly resolved backslopes can be simulated with sufficient fidelity to avoid processing artifacts.

#### G. Modulation of Ground Range Image Radiometry

Once DHM traversal is complete and the local illuminated area has been integrated over all desired points, the binary simulated radar image  $A_\gamma(r, a)$  is stored in memory. In the case of ground range images, one should at this stage adjust the areas stored to account for the fact that SAR processors generally create ground range images by resampling unmodulated *slant range* backscatter radiometry. Traversing the ground range raster, one modulates the contents with the nominal (ellipsoid model based) ratio of ground range to slant range reference areas

$$A_\gamma(g, a) \leftarrow A_\gamma(g, a) \cdot \delta_g(g) / \delta_r \quad (24)$$

Although the sensor's native slant range sample interval  $\delta_r$  is invariable, the equivalent ground range interval  $\delta_g(g)$  chosen by the SAR processor varies across the swath and is therefore a function of ground range  $g$ . Alternatively, one can perform the (24) modulation during the DHM traversal described previously.

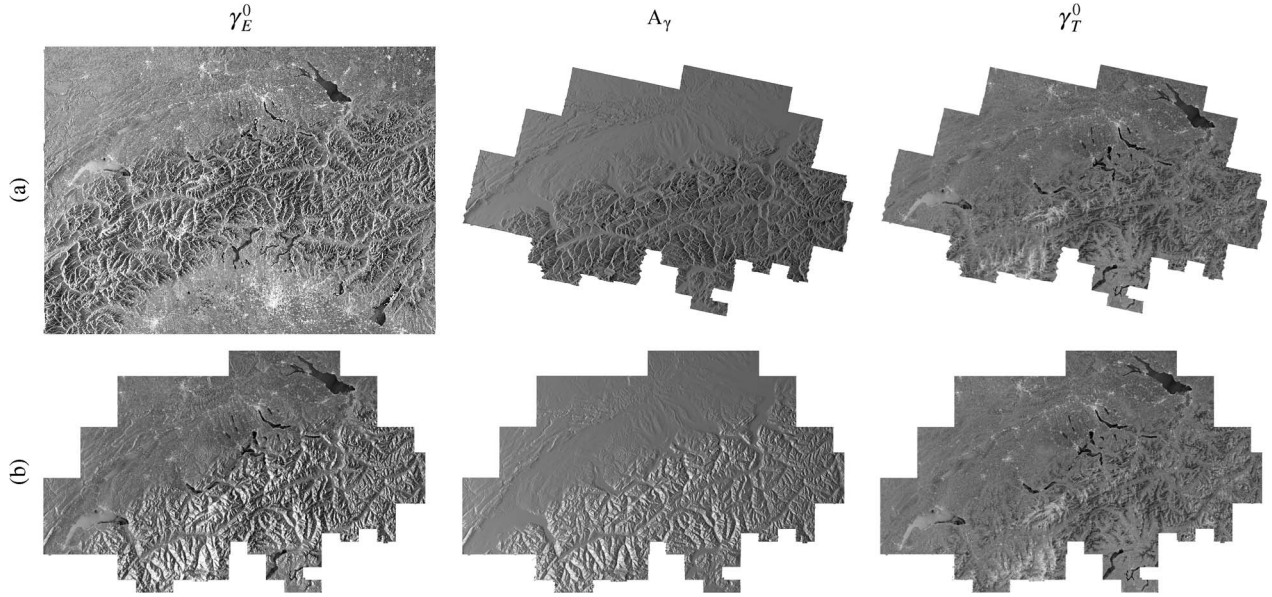


Fig. 8. ENVISAT ASAR WS VV Backscatter (25 dB dynamic range)—Image acquired over Switzerland on April 12, 2010: from left to right—Ellipsoid-based Gamma naught  $\gamma_E^0$ , Image simulation (reference area  $A_\gamma$ ), Terrain-based gamma naught  $\gamma_T^0$ —(a) Radar geometry, (b) Swiss oblique Mercator map geometry.

#### H. Buffer Output and Normalization

Whether in slant or ground range, the image simulation stored in memory as a radar geometry raster can then implement the inverse of the product's beta naught  $A_\beta$  normalization, producing an area factor estimate that may be applied directly for normalization

$$\hat{A}_\gamma(r, a) = A_\gamma(r, a)/A_\beta. \quad (25)$$

The final image simulation may then be written to a file with appropriate annotations. Normalization need not yet be performed at this stage: the image simulation, composed of local sums of illuminated area corresponding to each range and azimuth grid location can be output for use in other applications, such as, when necessary, refinement of the radar geometry [4], [15].

Once the radar geometry image simulation is available, it may be used (optionally) in a following step to normalize a real radar image for the systematic radiometric effects of topographic variations. Given a radar backscatter image presented in the  $\beta^0$  backscatter convention in radar geometry, the radiometrically terrain corrected (RTC) estimate of gamma backscatter is simply the backscatter divided by the local illuminated area

$$\gamma_T^0(r, a) = K_\gamma \cdot \frac{\beta^0(r, a)}{\hat{A}_\gamma(r, a)} \quad (26)$$

where  $r$  and  $a$  are the range and azimuth image coordinate, respectively and  $K_\gamma$  is a scalar calibration constant. Care is taken to avoid normalizing in areas where the local illuminated area is estimated to be zero (e.g., in areas of radar shadow) or below a threshold of 5% of the equivalent flatland area. A null cell value can be used to demarcate such image areas on the ragged edge of shadow. This normalized raster of  $\gamma_T^0$  estimates may then be geometrically corrected [9], just as one might terrain-geocode a slant range image of  $\gamma_E^0$  into a chosen map projection.

#### I. ENVISAT ASAR Wide Swath

An ASAR Wide Swath (WS) image covering Switzerland from April 2010 is used to illustrate intermediate processing levels of radiometric terrain correction in Fig. 8. ASAR wide swath “WSM” images have a nominal resolution of 120 m, delivering detected backscatter values in ground range geometry with nominal 75 m sample intervals in range and azimuth. The image simulation (and normalization) are generated initially in radar geometry (in this case a sliding ground range defined in the product annotations) at the WSM product's full resolution (no multi-looking was applied in RTC pre-processing). The image edges mark the limits of the swisstopo DHM25 height model that was used. The average accuracy of the DHM25 matrix model is advertised to be “1.5 m on the Swiss Plateau and in the Jura mountains, 2 m in the pre-Alps and the Canton of Ticino, and 3 m in the Alps” [20]. From left to right in Fig. 8(a) one sees ground range images showing ellipsoid-gamma  $\gamma_E^0$ , the reference area  $A_\gamma$  (image simulation), and terrain-flattened gamma  $\gamma_T^0$ . In the row below, Fig. 8(b) shows the same variables after terrain-geocoding. Note how the dark backscatter signature of wet snow is confounded with terrain-induced undulations in the  $\gamma_E^0$  GTC image. Better separation of the two effects is available in the  $\gamma_T^0$  image. Wet snow is visible as dark backscatter at intermediate Alpine altitudes, whereas melting had not yet begun at the higher elevations of the *Bernese Oberland* and the upper *Valais* in the southwest corner.

During terrain-geocoding, regions with relatively low illuminated area (mountain backslopes) “squeeze” into proportionally fewer samples, whereas foreslopes “stretch” into a wider space. It is for that reason that the image simulation  $A_\gamma$ 's backslopes are highlighted in ground range geometry, while the foreslopes appear more prominently in map geometry.

An example of terrain flattening performed using the SRTM3 height model is shown in Fig. 9. A standard full resolution ASAR WSM product acquired over southwestern British



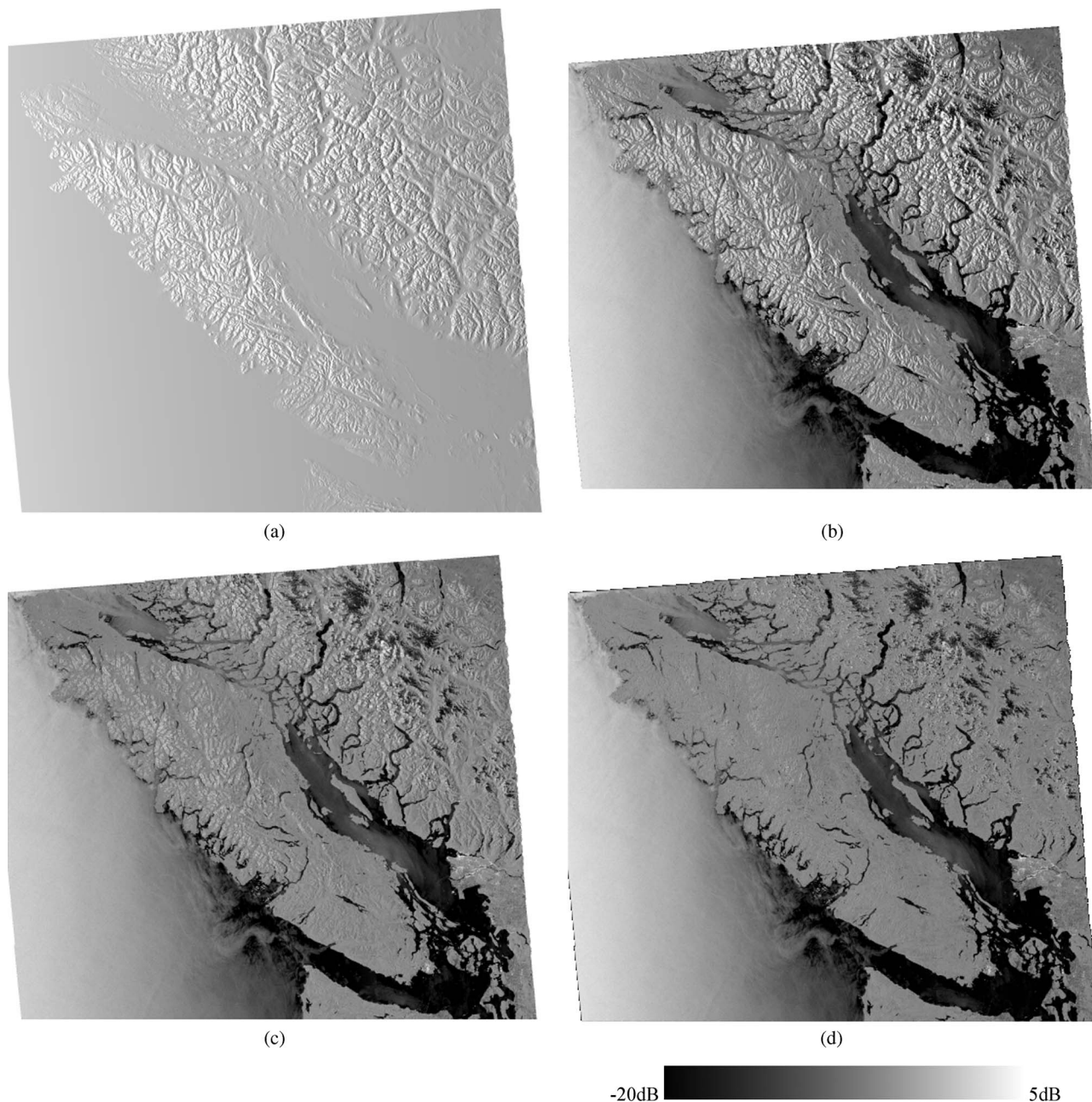


Fig. 9. ENVISAT ASAR Wide Swath VV Image acquired on 2008.09.10 of Vancouver Island and southwestern British Columbia, Canada—SRTM3 DHM used for terrain-geocoding and radiometric corrections. (a) Local contributing area  $A_\gamma$  (image simulation), (b)  $\gamma_E^0$  GTC, (c)  $\sigma_T^0 = \sigma_{NORLIM}^0$  NORLIM, (d)  $\gamma_T^0$  RTC.

Columbia, Canada was treated using SRTM3, generating gamma naught GTC and RTC products as well as sigma naught NORLIM. Previous results generated after  $2 \times 2$  multi-looking was performed in pre-processing were reported in [19]. In the following, no multi-looking was applied in radar geometry; the SRTM3 model was oversampled to a 50 m sample interval and the images were treated at the WSM product's native 75 m sample interval. The local contributing area  $A_\gamma$  is shown in Fig. 9(a),  $\gamma_E^0$  in Fig. 9(b),  $\sigma_T^0 = \sigma_{NORLIM}^0$  in Fig. 9(c), and  $\gamma_T^0$  in Fig. 9(d). The radiometric scale of 25 dB dynamic range is shared by all images. Note how the influence of terrain is confounded with land-cover effects in (b) and (c), but more clearly separated in (d), where the dark wet snow at high elevations is more distinct.

#### J. Local Incident Angle Fallacy

Conventional radiometric normalization procedures that rely on estimating the local incident angle [1], [10], [13], [23] to compute an appropriate local illuminated area fail to adequately model the sensor's measurement process and therefore perform relatively poorly in what is referred to as "challenging terrain." If not included in the sensor model, each of the following deficits will decrease the quality of the backscatter retrieval:

- 1) No check for local radar shadow is performed.
- 2) The estimate of local area is not projected into the plane perpendicular to slant range (gamma naught standard).

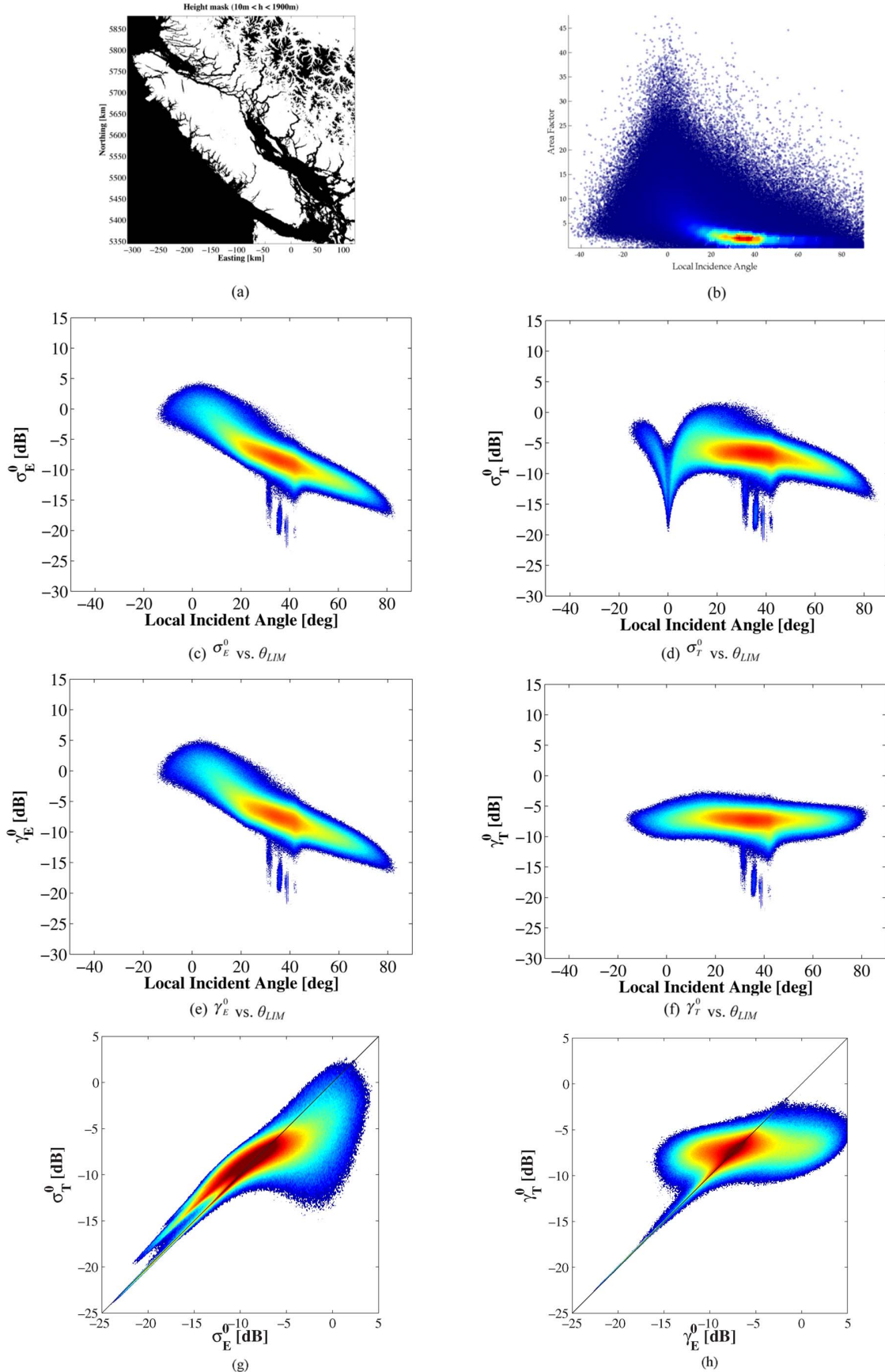


Fig. 10. Scatterplots quantitatively comparing different normalisation methods for ASAR WS image acquired over SW British Columbia, Canada: (a) intermediate height level mask for point selection, (b) area factor versus local incidence angle, (c)  $\sigma_E^0$  versus  $\theta_{LIM}$ , (d)  $\sigma_T^0$  versus  $\theta_{LIM}$ , (e)  $\gamma_E^0$  versus  $\theta_{LIM}$ , (f)  $\gamma_T^0$  versus  $\theta_{LIM}$ , (g)  $\sigma_T^0$  versus  $\sigma_E^0$ , (h)  $\gamma_T^0$  versus  $\gamma_E^0$ .



TABLE I  
SAR BACKSCATTER NORMALIZATION CONVENTIONS

Convention	1	2	3	4	5
Symbol	$\beta^0$	$\sigma_E^0$	$\gamma_E^0$	$\sigma_T^0$	$\gamma_T^0$
Earth Model	None	Ellipsoid		Terrain	
Reference Area	$A_\beta$	$\underline{A}_\sigma$	$\underline{A}_\gamma$	$\underline{A}_\sigma$	$A_\gamma$
Area Derivation	$\delta_a \cdot \delta_r$	$\delta_a \cdot \underline{\delta}_g$	$\delta_a \cdot \underline{\delta}_p$	$\delta_a \cdot \delta_g$	$\int_{DHM} \delta_a \cdot \delta_p$
Normalization	$\beta^0 = \beta / A_\beta$	$\sigma_E^0 = \beta^0 \cdot \frac{A_\beta}{\underline{A}_\sigma}$ $= \beta^0 \cdot \sin \theta_E$	$\gamma_E^0 = \beta^0 \cdot \frac{A_\beta}{\underline{A}_\gamma}$ $= \beta^0 \cdot \tan \theta_E$	$\sigma_T^0 = \beta^0 \cdot \frac{A_\beta}{A_\sigma}$ $= \sigma_E^0 \cdot \frac{\sin \theta_{LIM}}{\sin \theta_E}$	$\gamma_T^0 = \beta^0 \cdot \frac{A_\beta}{\int_{DHM} A_\gamma}$
Map-geometry product (when terrain-geocoded)	GTC			NORLIM	RTC

- 3) One of the two triangular DHM facets inherent to neighbors in a raster elevation model is ignored, throwing away information inherently available from the DHM.
- 4) The azimuth component of variations in the illuminated areas of the two facets (and its co-dependence on range variations) is ignored.
- 5) The non-homomorphic nature of the relationship between slant range geometry and the map geometry of the DHM is not modeled—or if it is, relatively low-fidelity nearest neighbor distribution of the facet area from map to radar geometry blurs spatial focus.
- 6) In ground range products, no compensation for the fact that the radiometry remains slant-range based is implemented. Local area image simulations need to mimic the behavior of SAR processors to provide an appropriate image reference. This last point is irrelevant for slant-range products.

Users should be aware of any of the above deficiencies in their backscatter retrieval software to understand the limitations it may have in regions of “challenging” terrain.

In the following, the ASAR WS scene from Fig. 9 is used to quantitatively compare the relative flatness achieved by the  $\sigma_T^0$  versus  $\gamma_T^0$  methodologies. The site was chosen “based on its relatively homogenous land cover (conifers) to minimize confounding effects from height-dependent natural land-cover variations” [19]. To further minimize land-cover heterogeneity, ocean areas subject to Bragg scattering ( $h < 10$  m) and high mountain peaks subject to snowmelt ( $h > 1900$  m) were excluded—the resulting selection mask is shown in Fig. 10(a).

The magnitude of the disagreement between local incident-angle mask based approaches and the  $\gamma_T^0$  retrieval introduced here is illustrated in a density plot in Fig. 10(b). There is clearly no one-to-one relationship between local illuminated area and

incident angle, even if some correlation is visible. Indeed, one sees that the ratio of areas at a single incident angle can be 40 or even higher (16 dB).

A scatterplot of  $\sigma_E^0$  versus  $\theta_{LIM}$  is shown in Fig. 10(c). Terrain-flattened sigma naught retrieved via NORLIM is juxtaposed to the right as  $\sigma_T^0$  versus  $\theta_{LIM}$  in Fig. 10(d). The density scales are logarithmic, indicating the relative number of points found at each coordinate. Points within the selection mask shown in Fig. 10(a) were included. Note the singularity that appears at  $0^\circ$  incident angle: the NORLIM “normalization” multiplies by the sine of  $0^\circ$ , destroying information: use of angle as a proxy induces an estimate of “infinite” local contributing area at that slope: clearly a suboptimal use of the available DHM information.

An equivalent plot of the other ellipsoid-based backscatter retrieval method (gamma)  $\gamma_E^0$  is shown in Fig. 10(e); the behavior is similar to  $\sigma_E^0$ . By adopting measurement of area directly rather than use of an angular proxy, the scatterplot of  $\gamma_T^0$  versus  $\theta_{LIM}$  in Fig. 10(f), shows no singularity. Instead,  $\gamma_T^0$  values stay flat through  $0^\circ$  incident angle: compare (d) and (f). In addition, the variability is also significantly reduced in the RTC in comparison to the NORLIM retrieval. The performance of the backscatter retrieval algorithms represented by  $\sigma_T^0$  and  $\gamma_T^0$  are compared in (g) and (h). Ellipsoid-based  $\sigma_E^0$  is plotted against  $\sigma_T^0$  in (g). As reported using coarser multi-look data [19], the NORLIM “flattening” *spreads* relatively  $\sigma_E^0$  bright values (predominantly on foreslopes) into a *wider* range of  $\sigma_T^0$  values, alternately over- and under-compensating for the effects of terrain. In the *mean*, low backscatter values are raised, and high backscatter values dampened, but one must average over wide areas (e.g.,  $5 \times 5$  as reported in [10]) for this to be reliably applicable locally. In comparison to the multi-looked data presented in [19], the effects of the  $0^\circ$  singularity are slightly less severe in the results reported here, as slopes were

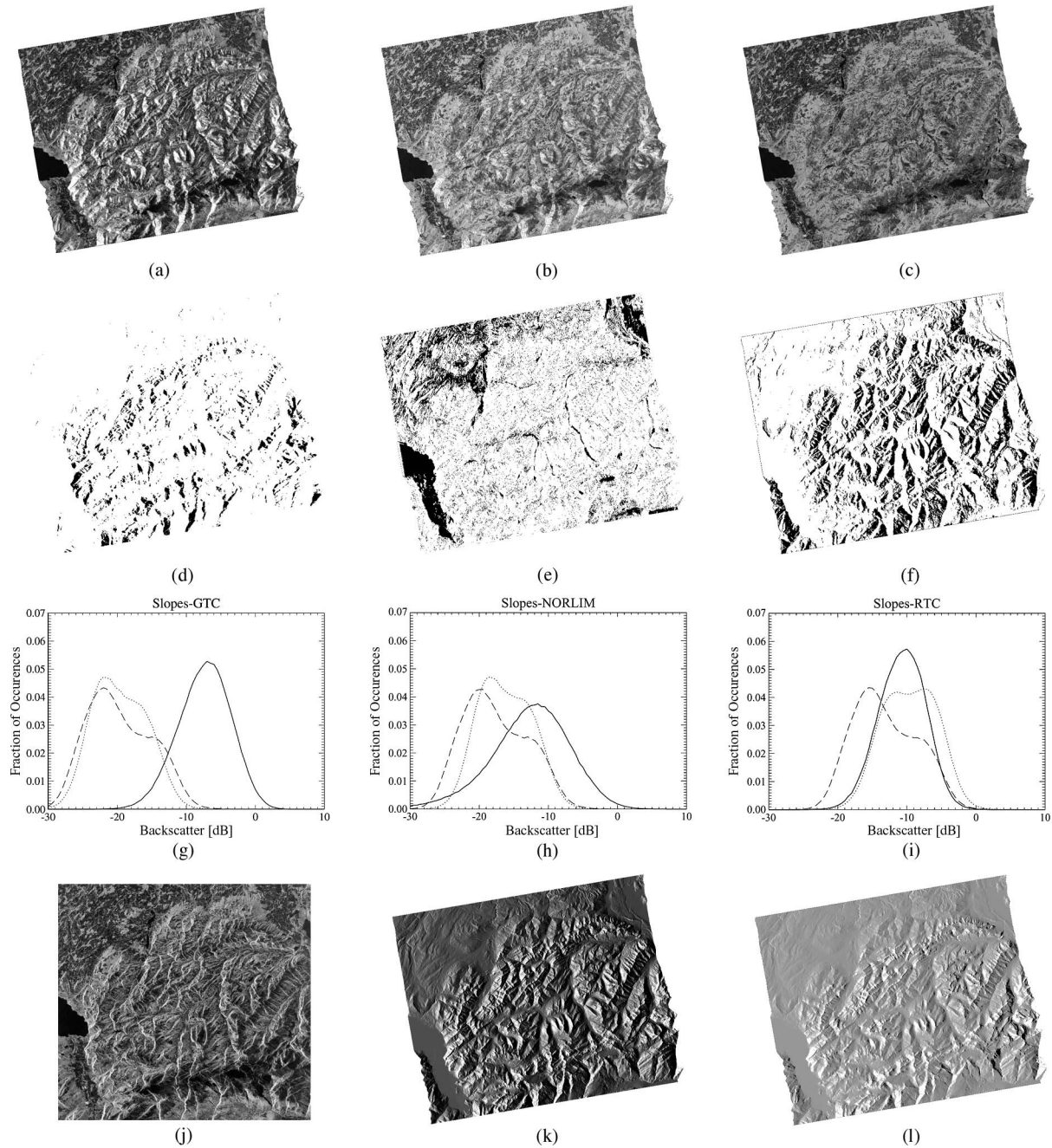


Fig. 11. ALOS PALSAR FBD HV—Fribourg, Switzerland—June 19, 2008. Backscatter scaled to 20 dB dynamic range (a) GTC  $\gamma_T^0$ , (b) NORLIM  $\sigma_T^0$ , (c) RTC  $\gamma_T^0$ ; Masks indicating (d) foreslopes, (e) flat, (f) backslopes; Histograms in (g)–(i) show foreslope (solid), flat (dashed), backslope (dotted) for GTC, NORLIM, RTC; (j) Slant range detected input image, (k) Local incident angle mask, (l) Local reference area image simulation.

calculated using a more densely sampled 50 m DHM. The terrain-flattened gamma naught values plotted in (h) indicate that its backscatter retrieval was able to squeeze  $\gamma_E^0$ 's relatively wide distribution into a significantly more compact range of  $\gamma_T^0$  values. Note that the identical points from the mask in Fig. 10(a) were used to generate the plots of  $\sigma_T^0$  and  $\gamma_T^0$  in (d) and (f). The logarithmic scale for relative density indicates that, as easily verified in Fig. 9(d), most  $\gamma_T^0$  retrievals restrict themselves to a relatively narrow range of values.

Broadly, incident angle-based terrain-flattening approaches could be described as *sigma naught normalization*. They assume backscatter to be dependent on the local ground area, and

perform best in lightly rolling hills with slowly varying slopes that never venture into territory subject to severe foreshortening. Rather than sigma naught, the methodology introduced here is constructed instead for *gamma naught normalization*. Although a more highly evolved sensor model is required to flatten gamma, one is rewarded with more robust backscatter retrieval.

During the acquisition of a SAR image, the sensor's transmitted pulses are convolved with the landscape, and the resulting echoes are recorded—that convolution needs to be replicated in the sensor model used for backscatter normalization. Layover areas need not be “masked out” [8]: as the convolution results



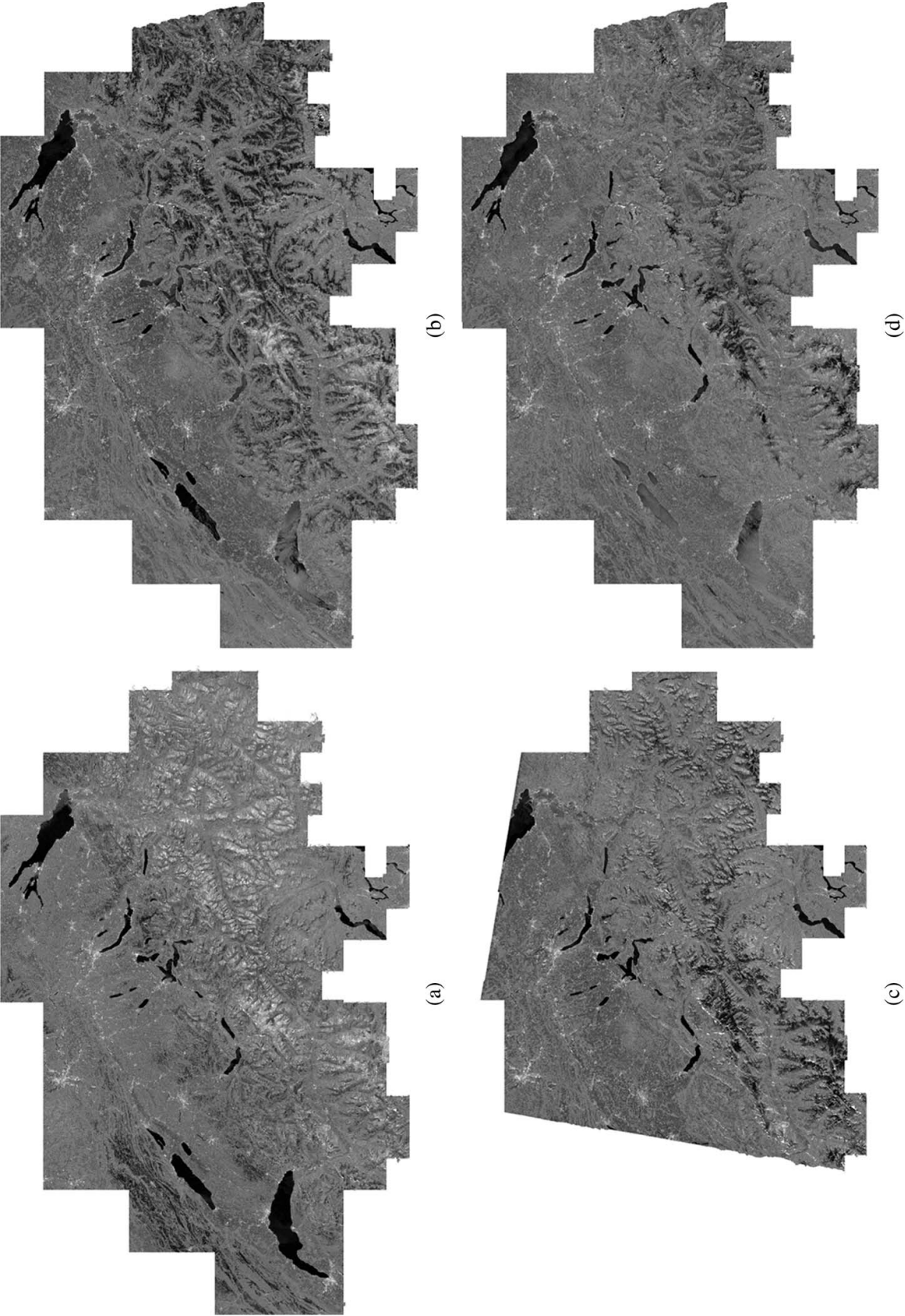


Fig. 12. ENVISAT ASAR Wide Swath VV-polarization RTC backscatter images of Switzerland from multiple tracks. -20 dB (black) to 5 dB (white). (a) March 17, 2009 descending; (b) April 11, 2009 ascending; (c) May 23, 2009 descending; (d) June 20, 2009 ascending.



in the addition of many contributions along a foreslope, the *integration step* within the image simulation mimics the behavior in its sensor model, generating the single (relatively large) local reference area that is appropriate. No explicit special case is activated within the image simulation when dealing with layover (or foreshortened) areas: the good performance is rather a consequence of a better simulation of the actual convolution with the landscape. A special case *is* invoked in shadowed areas: they are excluded from contributing to the running sum of local reference area, with the same motivation: to better replicate the behavior of the convolution of the SAR's pulse with the landscape. As no echo is returned from shadowed areas, the local DHM facet's area in shadow is irrelevant to the normalization and should be ignored. Shadowed areas are inaccessible to backscatter retrieval, due to the lack of availability of a measurement.

The manner in which elevation antenna pattern (EAP) variations are draped across the elevation model may also be integrated into the image simulation process if a model of the EAP is available. An example of such correction is reported in [6]. Note that the influence of EAP terrain variations is usually orders of magnitude less strong than that of the area variation [16].

Table I summarizes the four widespread backscatter conventions, beta, sigma, and gamma naught, as well as local-incident angle flattened sigma naught, listing the reference area used for backscatter normalization, and showing how each is calculated. As proposed in [17], it adds terrain-flattened gamma as a fifth option for users that require robust backscatter retrieval in areas with terrain variations.

### III. TERRAIN-FLATTENED GAMMA

#### A. Performance

This section shows comparisons of terrain flattened  $\gamma_T^0$  with conventional normalization methods under a variety of conditions. Fig. 11 compares the performance of each method on an ALOS PALSAR FBD HV image acquired just east of Lake Geneva in Switzerland on June 19, 2008. The PALSAR FBD slant range complex "L1.1" product was acquired at a nominal incident angle of  $38.7^\circ$  and generated with sample intervals of 9.4 m in slant range and 3.5 m in azimuth. It was detected and reduced to nominally "square" (as measured in ground range) image pixels by taking one range look and four azimuth looks. The swisstopo DHM25 height model [20] was used throughout.

Fig. 11(a)–(c) show terrain-geocoded  $\gamma_E^0$ ,  $\sigma_T^0$ , and  $\gamma_T^0$  images, respectively. One sees that the NORLIM slope correction in (b) dampens the strong backscatter from foreslopes seen in (a), but not nearly as well as the RTC normalization in (c), where forest/non-forest boundaries become clear. Dark backscatter is visible from wet snow on high mountains in the south. Fig. 11(d)–(f) show masks demarcating foreslope, flat, and backslope regions within the image. Histograms of backscatter estimates made using GTC, NORLIM, and RTC images are shown in Fig. 11(g)–(i). The solid line shows *foreslopes*, the dashed line *flat* regions, and the dotted line *backslopes*. As expected, the widest dispersion is in the GTC imagery; RTC normalization is able to brighten the backslopes

and dampen the foreslope backscatter so that nearly all returns are between  $-20$  dB and  $0$  dB. The NORLIM method applying (5) is seen to be less successful in this regard, blurring the foreslope return over a wide range due to its lack of a heteromorphic model. More surprisingly, it also fails to significantly brighten the backslope regions, probably due to its assumption of the  $\sigma^0$  convention's ground area directly determining backscatter energy. In contrast, the RTC normalization is based on the  $\gamma^0$  definition of ground area projected in the plane perpendicular to slant range, and brightens the backslopes so well that the forest/non-forest boundary is consistently visible on both sides of the Rhone valley just south of Lake Geneva, across strong fore/backslope boundaries. For GTC, NORLIM, and RTC, the dark return from the flat Lake Geneva in the west of the image causes a multimode distribution in the flat case.

The slant range detected image in Fig. 11(j) illustrates the strength of the foreshortening present in the scene. The local incident angle mask in Fig. 11(k) is juxtaposed next to the RTC normalization area (image simulation) in Fig. 11(l). Although the two images appear superficially similar at this image scale, the histograms illustrate that their use in normalization is far from equivalent. Higher resolution versions of the images in Fig. 11(a)–(c) are available in [18].

#### B. Spring Snow Melt

The use of radiometric terrain correction promises to be of great utility in tracking wet snow backscatter signatures in mountainous terrain. ASAR wide swath  $\gamma_T^0$  images illustrate the existing potential in Fig. 12. Four images from 2009 (March to June) show the progressive seasonal rise in snow melt altitude as the spring season progresses. Comparing the images to one another directly, one might at first hardly notice that two were acquired in an ascending, and two in a descending orbital configuration (also different tracks). Such direct comparison of GTC images would be impossible—without normalization, the thematic wet snow signature is confounded with *individual* track-dependent *terrain backscatter*, not the *terrain-cover* backscatter that is the object of study.

### IV. CONCLUSION

Accurate annotation of a SAR platform's position and timing parameters enables not only *terrain geocoding*, that is, overlays in map geometry of images acquired in different modes, look directions, even by different sensors. It also enables estimation of systematic terrain-induced *radiometric* effects, and normalization for local illuminated area. The normalization factor is best estimated directly as an area, without resort to intermediate local incident and azimuth angles. A multifaceted approach is better able to capture the actual backscatter measurement process within its sensor model, and improve the quality of the backscatter retrieval.

A methodology for a radiometric normalization scheme more robust than that available in the literature has been presented. More widespread application of the technique would allow deeper analysis of the large archive of radar data covering hilly to mountainous areas, enabling multi-track comparisons

with far denser temporal sampling rates. Radiometric terrain correction is also a prerequisite for multi-sensor comparisons [17] over such areas, as the imaging geometries inherent to each sensor almost always differ significantly. It shows great potential for improving SAR-based mapping of wet snow in mountainous areas, e.g., at the time of spring snow melt.

#### ACKNOWLEDGMENT

This work was supported in part by the European Space Agency under ESRIN/Contract No. 22501/09/I-EC. The ENVISAT ASAR data was provided by ESA. The ALOS PALSAR data was provided by JAXA through ESA's ADEN node for cal/val and as part of project AO3600. The digital height model DHM25 from swisstopo was used to generate the image simulations covering the area of Switzerland. The SRTM3 digital surface model was used elsewhere. Assistance from Dr. Adrian Schubert (RSL) for DHM preparation and Lukas Zuberbühler (RSL) with density plots as well as fruitful discussions with Adrian & Lukas, Dr. Erich Meier (RSL) and Nuno Miranda (ESA) are gratefully acknowledged.

#### REFERENCES

- [1] T. Bayer, R. Winter, and G. Schreier, "Terrain influences in SAR backscatter and attempts to their correction," *IEEE Trans. Geosci. Remote Sens.*, vol. 29, no. 3, pp. 451–462, May 1991.
- [2] Information on ALOS PALSAR Products for ADEN Users, ESA, Frascati, Italy, Apr. 5, 2007, ALOS-GSEG-EOPG-TN-07-0001.
- [3] D. J. Goering, H. Chen, L. D. Hinzman, and D. L. Kane, "Removal of terrain effects from SAR satellite imagery of arctic terrain," *IEEE Trans. Geosci. Remote Sens.*, vol. 33, no. 1, pp. 185–194, Jan. 1995.
- [4] B. Guindon and M. Adair, "Analytic formulation of spaceborne SAR image geocoding and 'value-added' product generation procedures using digital elevation data," *Can. J. Remote Sens.*, vol. 18, no. 1, pp. 2–12, Jan. 1992.
- [5] M. Hinse, Q. H. J. Gwyn, and F. Bonn, "Radiometric correction of C-band imagery for topographic effects in regions of moderate relief," *IEEE Trans. Geosci. Remote Sens.*, vol. 26, no. 2, pp. 122–132, Mar. 1988.
- [6] F. Holecz, A. Freeman, and J. van Zyl, "Topographic effects on the antenna gain pattern correction," in *Proc. IGARSS*, Florence, Italy, 1995, pp. 587–589.
- [7] J. M. Kellndorfer, M. Pierce, C. Dobson, and F. Ulaby, "Toward consistent regional-to-global-scale vegetation characterization using orbital SAR systems," *IEEE Trans. Geosci. Remote Sens.*, vol. 36, no. 5, pp. 1396–1410, Sep. 1998.
- [8] A. Löw and W. Mauser, "Generation of geometrically and radiometrically terrain corrected SAR image products," *Remote Sens. Environ.*, vol. 106, no. 3, pp. 337–349, Feb. 2007.
- [9] E. Meier, U. Frei, and D. Nüesch, "Precise terrain corrected geocoded images," in *SAR Geocoding: Data and Systems*, G. Schreier, Ed. Karlsruhe, Germany: Herbert Wichmann Verlag GmbH, 1993.
- [10] D. Pairman, S. Belliss, and S. McNeill, "Terrain influences on SAR backscatter around Mt. Taranaki, New Zealand," *IEEE Trans. Geosci. Remote Sens.*, vol. 35, no. 4, pp. 924–932, Jul. 1997.
- [11] K. Raney, A. Freeman, B. Hawkins, and R. Bamler, "A plea for radar brightness," in *Proc. IGARSS*, Pasadena, CA, 1994, pp. 1090–1092.
- [12] B. Rosich and P. Meadows, "Absolute calibration of ASAR level 1 products generated with PF-ASAR," ESA-ESRIN, Frascati, Italy, ENVICLV-EOPG-TN-03-0010, 2004, Issue 1, Revision 5.
- [13] M. Shimada and H. Hirose, "Slope corrections to normalized RCS using SAR interferometry," *IEEE Trans. Geosci. Remote Sens.*, vol. 38, no. 3, pp. 1479–1484, May 2000.
- [14] M. Shimada, O. Isoguchi, T. Tadono, and K. Isono, "PALSAR radiometric and geometric calibration," *IEEE Trans. Geosci. Remote Sens.*, vol. 47, no. 12, pp. 3915–3932, Dec. 2009.
- [15] D. Small, S. Biegger, and D. Nüesch, "Automated tie point retrieval through heteromorphic image simulation for spaceborne SAR sensors," in *Proc. ESA ERS-ENVISAT Symp.*, Gothenburg, Sweden, 2000.
- [16] D. Small, M. Jehle, E. Meier, and D. Nüesch, "Radiometric terrain correction incorporating local antenna gain," in *Proc. 5th EUSAR*, Ulm, Germany, 2004.
- [17] D. Small, N. Miranda, and E. Meier, "A revised radiometric normalization standard for SAR," in *Proc. IGARSS*, Cape Town, South Africa, 2009, pp. 566–569.
- [18] D. Small, N. Miranda, and E. Meier, "Local incidence angle considered harmful," in *Proc. CEOS SAR Cal/Val Workshop*, Pasadena, CA, Nov. 17–19, 2009.
- [19] D. Small, N. Miranda, L. Zuberbühler, A. Schubert, and E. Meier, "Terrain-corrected Gamma: Improved thematic land-cover retrieval for SAR with robust radiometric terrain correction," in *Proc. ESA Living Planet Symp.*, Bergen, Norway, Jul. 2010, ESA Special Publication SP-686, 8 p.
- [20] swisstopo, *DHM25: The Digital Height Model of Switzerland—Product Information*, Jun. 2005, 15 p.
- [21] F. T. Ulaby, R. Moore, and A. Fung, *Microwave Remote Sensing: Active and Passive Vol. II: Radar Remote Sensing and Surface Scattering and Emission Theory*. Norwood, MA: Artech House, 1982, p. 463.
- [22] L. Ulander, "Radiometric slope correction of synthetic-aperture radar images," *IEEE Trans. Geosci. Remote Sens.*, vol. 34, no. 5, pp. 1115–1122, Sep. 1996.
- [23] J. J. van Zyl, B. Chapman, P. Dubois, and J. Shi, "The effect of topography on SAR calibration," *IEEE Trans. Geosci. Remote Sens.*, vol. 31, no. 5, pp. 1036–1122, Sep. 1993.



**David Small** (S'86–M'98) was born in Ontario, Canada. He received the B.A.Sc. degree in systems design engineering from the University of Waterloo, Waterloo, ON, Canada, in 1988, the M.A.Sc. degree in electrical engineering from the University of British Columbia (UBC), Vancouver, BC, Canada, in 1991, and the Ph.D. degree from the University of Zürich (UZH), Zürich, Switzerland, in 1998.

He is currently a Senior Research Scientist and Co-Leader of the SAR group within the Remote Sensing Laboratories of the University of Zürich. In

the past, he has researched improvements to generation of height models using cross-track radar interferometry, and geometric calibration and validation for a variety of SAR sensors. He is presently researching the extension of radar image simulation software to incorporate further mode-specific parameterizations and monitor systematic signatures of snow melt over large areas. He is a member of the European Space Agency's Quality Working Group for SAR sensors.

Dr. Small is a member of the IEEE-GRS Society. He was chair of the CEOS SAR calibration/validation workshop in 2010.